

RESEARCH ARTICLE

CARBON CAPTURE

A scalable metal-organic framework as a durable physisorbent for carbon dioxide capture

Jian-Bin Lin^{1†}, Tai T. T. Nguyen², Ramanathan Vaidhyanathan^{1,3}, Jake Burner⁴, Jared M. Taylor^{1,5}, Hana Durekova⁴, Farid Akhtar⁶, Roger K. Mah^{1,5}, Omid Ghaffari-Nik⁷, Stefan Marx⁸, Nicholas Fylstra¹, Simon S. Iremonger¹, Karl W. Dawson¹, Partha Sarkar², Pierre Hovington^{7*}, Arvind Rajendran^{2*}, Tom K. Woo^{4*}, George K. H. Shimizu^{1,5*}

Metal-organic frameworks (MOFs) as solid sorbents for carbon dioxide (CO₂) capture face the challenge of merging efficient capture with economical regeneration in a durable, scalable material. Zinc-based Calgary Framework 20 (CALF-20) physisorbs CO₂ with high capacity but is also selective over water. Competitive separations on structured CALF-20 show not just preferential CO₂ physisorption below 40% relative humidity but also suppression of water sorption by CO₂, which was corroborated by computational modeling. CALF-20 has a low enthalpic regeneration penalty and shows durability to steam (>450,000 cycles) and wet acid gases. It can be prepared in one step, formed as composite materials, and its synthesis can be scaled to multikilogram batches.

Capture of CO₂ after fossil fuel combustion requires CO₂ removal from a localized emission source but also regeneration and recycling of the capture system. Major challenges for the capture stage span materials design and development through to process engineering (1, 2). Flue gas has a low concentration of CO₂ diluted in mostly N₂ along with water and acid gases (3). Amine and solvent systems (4, 5) rely on contacting flue gas with a liquid that absorbs the CO₂ through a combination of chemical and physical absorption. Although CO₂ removal is effective, regeneration is energy intensive and can lead to chemical decomposition (6).

Solid sorbents represent a step-change technology for carbon capture (7–10) and have been demonstrated at smaller scales (11). Solids can bind CO₂ through either chemical or physical sorption (3, 7–10). In most cases, chemisorptive materials have higher capacity and selectivity for CO₂ (12). However, factors that enhance CO₂ binding often proportionally increase the energy needed to regenerate the sorbent and can enhance binding of competing gases. For the absolute CO₂ uptake, the relevant parameter

is working capacity under the operational cycling conditions to regenerate the solid sorbent (3). Selectivity over N₂ is typically reported, but sorption of CO₂ in the presence of water vapor is much less reported, especially for physisorptive capture systems (12–14). A physisorptive CO₂ capture solid would offer much lower regeneration costs, but it must have sufficient working capacity and selectivity in an actual flue stream in which gases are present with stronger intermolecular attractive forces than those of CO₂. Moreover, to translate to process productivity, the kinetics of sorption and release are as important as capacity.

Nearly all classes of porous solids have potential as solid sorbents for CO₂ capture (1–3, 7–10), including metal-organic frameworks (MOFs) (2, 3, 9, 12–14), in which chemical building blocks, pore sizes and shapes, surface functionalities, and even degrees of order can be varied to optimize CO₂ capture ability. More robust MOFs (15, 16), including ones that are stable in the presence of water (17–19) and steam (20), have been reported, although stability to wet acid gases is less common (21–23). For sorbent powder to be a usable material, it must be capable of formation in macroscopic shape for rapid mass transfer and thermal management, be durable in that form, and be available at scale (hundreds of thousands of tonnes) and reasonable cost (24, 25).

Solid sorbents optimized in an adsorption process have the potential to substantially decrease the CO₂ capture cost compared with traditional amine absorption processes because of lower regeneration energy, less chemical decomposition versus the solvent capture system, extensive use of stainless-steel owing to the corrosivity of amine solvents, and large plant footprint (4–6). Optimization of the solid sorbent

process must include high volumetric productivity in the presence of water (present in the flue gas) and the lowest regeneration energy. For regeneration, several processes are under evaluation, including vacuum swing, pressure swing, and temperature swing (26). Although cycling performance per sorbent volume or productivity is one of the main drivers of final CO₂ capture cost, there are several other parameters that affect operating and capital expenses of CO₂ capture. For solid sorbents, unlike solvent-based absorption, it is not feasible to continuously replace deactivated sorbents with fresh ones.

Here we present Calgary Framework 20 (CALF-20), a MOF with high capacity and selectivity for CO₂ despite a physisorptive mechanism and modest heat of adsorption. Its selectivity extends beyond N₂ to capture CO₂ in a wet gas. CALF-20 is exceptionally robust and stable to steam, wet acid gases, and even prolonged exposure to direct flue gas from natural gas combustion. Its single-step synthesis from commercially available components is highly scalable. The origin of the CO₂ philicity, despite CALF-20 being highly water resistant, was studied by simulation. Structuring of CALF-20 was performed, as well as competitive breakthrough experiments in wet gas streams that aligned with pure-component isotherms, heats of adsorption, and molecular modeling. In particular, not only can CALF-20 physisorb CO₂ up to and beyond 40% RH, but the presence of CO₂ actually suppresses water sorption. Finally, we present durability and CO₂ capture data on the MOF that are based on industrial testing.

Synthesis, structure, and gas sorption

CALF-20, [Zn₂(1,2,4-triazolate)₂(oxalate)], was initially prepared solvothermally and single crystals obtained through the in situ degradation of a dihydroxybenzoquinone derivative (see supplementary materials). CALF-20 is composed of layers of 1,2,4-triazolate-bridged zinc(II) ions pillared by oxalate ions to form a three-dimensional (3D) lattice and 3D pore structure (Fig. 1, A to C). Channels of 2.73 Å by 2.91 Å, 1.94 Å by 3.11 Å, and 2.74 Å by 3.04 Å along [100], [011], and [0 $\bar{1}$ 1], respectively (factoring van der Waals radii), that permeate the MOF result in a ~38% void volume. The one crystallographically unique Zn center is five-coordinate with a distorted trigonal bipyramidal geometry [Zn–O = 2.022(2), 2.189(3) Å; Zn–N = 2.007(2), 2.016(3), 2.091(3) Å]. The N atoms in the 1,2 positions of the triazolate bridge Zn dimers are linked to the next dimer by the N atom in the 4-position. The Zn coordination is completed by two oxygen atoms of a chelating oxalate group, and there are no open coordination sites. The bulk powder shows the same phase (Fig. 1D). Detailed structural analyses on pillared zinc triazolates have shown that layers can exist

¹Department of Chemistry, University of Calgary, Calgary, Alberta, Canada. ²Department of Chemical and Materials Engineering, University of Alberta, Edmonton, Alberta, Canada. ³Indian Institute of Science Education and Research, Dr. Homi Bhabha Road, Pashan, Pune, Maharashtra, 411008, India. ⁴Department of Chemistry and Biomolecular Science, University of Ottawa, Ottawa, Ontario, Canada. ⁵ZoraMat Solutions Inc., Calgary, Alberta, Canada. ⁶Department of Materials Engineering, Luleå University of Technology, Luleå, Sweden. ⁷Svante Inc., Vancouver, British Columbia, Canada. ⁸BASF SE, Ludwigshafen am Rhein, Germany.

*Corresponding author. Email: phovington@svanteinc.com (P.H.); arvind.rajendran@ualberta.ca (A.R.); twoo@uottawa.ca (T.K.W.); gshimizu@ucalgary.ca (G.K.H.S.)

[†]Present address: C-CART, CREAT Network, Memorial University of Newfoundland, St. John's, Newfoundland and Labrador, Canada.

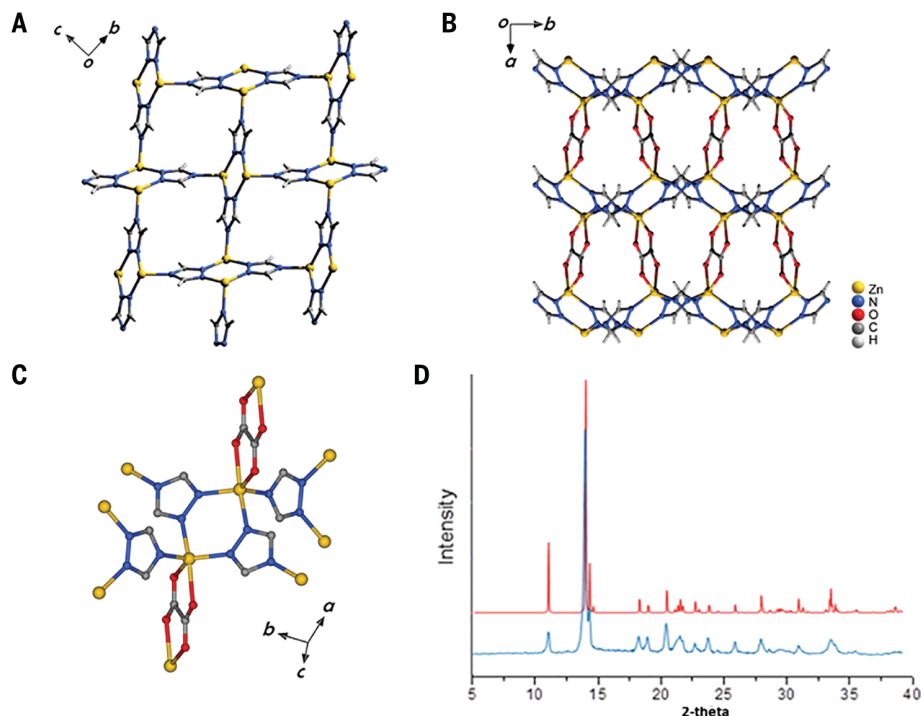


Fig. 1. Single-crystal structure of CALF-20. (A) View of the two-dimensional zinc triazolate grid. (B) View orthogonal to (A) showing the pillaring of the zinc triazolate layers by oxalate anions. (C) View of the zinc coordination sphere (H atoms removed). (D) Powder x-ray pattern simulated from the single-crystal structure (top) and obtained experimentally.

in different manifestations with varying degrees of buckling (27, 28). Indeed, since a provisional patent application was filed in 2014, a hydrated form of $[\text{Zn}_2(1,2,4\text{-triazolate})_2(\text{oxalate})]$ has been reported (29). This structure has the same connectivity but slightly different unit cell and pore dimensions. The specific pore structure affects sorption properties, and modeling was carried out with our obtained crystal data.

Gas adsorption experiments were performed for CO_2 and N_2 (Fig. 2A). The Langmuir surface area calculated from the N_2 isotherm at 77 K was $528 \text{ m}^2 \text{ g}^{-1}$, and the uptake for CO_2 was 4.07 mmol g^{-1} at 1.2 bar and 293 K. The zero-loading heat of adsorption for CO_2 was -39 kJ mol^{-1} (fig. S6), and the calculated selectivity for CO_2/N_2 by ideal adsorbed solution theory was 230 for a 10:90 CO_2/N_2 mixture. CALF-20 structured readily as a 20% polysulfone composite and retained the expected porosity (Fig. 2, B and C, and fig. S5). For CO_2 capacity and selectivity over N_2 as metrics, there are numerous other materials with noteworthy performance (30–36). The water sorption profile of CALF-20 was unusual in that, for a solid with good physisorptive capacity for CO_2 , it exhibited poor water uptake at low partial pressures (Fig. 2, D and E). Comparisons to zeolite 13X (37), as well as two other water-resistant MOFs, CAU-10 (38) and Al fumarate (39), are included in Fig. 2 and fig. S16. Moreover, higher-temperature

water isotherms showed that water uptake decreased more readily at higher temperatures than did the corresponding CO_2 isotherms.

Binding-site modeling

To gain insights into the nature of CO_2 binding in CALF-20 and its unusual water sorption behavior, we performed atomistic grand canonical Monte Carlo (GCMC) simulations (see supplementary materials). The experimental and simulated CO_2 and N_2 isotherms were in excellent agreement (see supplementary materials). Probability distributions of the guest molecules within the MOF allowed us to identify binding sites. The most probable CO_2 binding, which lies in the middle of the CALF-20 pore (Fig. 3A), had a binding energy of $-34.5 \text{ kJ mol}^{-1}$ based on the GCMC force field; the density functional theory (DFT) value with dispersion corrections was $-36.5 \text{ kJ mol}^{-1}$. The interatomic distances displayed were consistent with physisorption; the shortest distance was 3.03 \AA between the CO_2 oxygen and a hydrogen of the triazole (fig. S8). Analysis of the binding energy revealed that the CO_2 -MOF interaction was dominated by attractive dispersion interactions (85%), with electrostatics contributing the balance.

Water adsorption isotherms are more challenging to simulate given the polar nature of water, which enables potentially strong interactions with the framework and with itself. The experimental water isotherm had a general

S-shape, where the water uptake was initially low until $\sim 10\%$ relative humidity (RH), at which point there was a steep rise until $\sim 30\%$ RH (Fig. 3B). These features indicated that water condensed in the pores, and they were reproduced in the simulated isotherm. After the initial steep rise in water uptake beyond 30% RH, the experimental isotherm showed a more gradual increase in adsorption until reaching a saturation limit at $\sim 11 \text{ mmol g}^{-1}$. However, for the simulated isotherm, the steep rise continued until full saturation at 40% RH and then flattened. The general S-shape and the saturation capacity of $\sim 11 \text{ mmol g}^{-1}$ were reproduced by the simulation.

A snapshot from the pure water simulation at 20% RH, where the water uptake was roughly half the saturation limit (Fig. 3C), revealed that the pores were either full of water molecules, forming a hydrogen-bonded network, or completely empty. In comparison, at 60% RH, where uptake had fully saturated, all the pores were full of hydrogen-bonded water molecules (fig. S9). The equilibrium distribution at 20% RH, where partially filled pores were not observed, suggested rapid condensation or evaporation of water. We extracted the water binding sites at 20% RH with the highest probability from the GCMC simulations, and the top three binding sites, in order, are labeled i, ii, and, iii in Fig. 3D. The binding energies with the framework of the sites, -17.5 , -8.9 , and $-29.1 \text{ kJ mol}^{-1}$, respectively, were calculated by placing a single water molecule in the site with no other guest molecule present. The two most probable binding sites had a relatively low binding energy and were oriented away from the framework such that there were no hydrogen-bonding interactions with the oxalate linkers. Water molecules in these sites were poised to form hydrogen-bonding interactions with other water molecules, which suggested that the main driver for the initial water uptake was the interaction with other water molecules. This result was consistent with the experimentally observed water-uptake properties of CALF-20 at low RH.

Breakthrough studies

The intriguing CO_2 and water isotherms prompted a series of dynamic breakthrough studies (Fig. 4) on the CALF-20-polysulfone composite (see supplementary materials). Competitive CO_2/N_2 studies, with CO_2/N_2 mixtures of 5/95, 15/85, and 30/70, respectively (Fig. 4, A and B), confirmed the selectivity suggested by the pure-component isotherms. In the N_2 profiles, a sharp front, indicating complete breakthrough of N_2 , was observed at dimensionless time (ratio of experimental time to the time taken by a nonadsorbing tracer to travel through the column) $\bar{t} \sim 4$ in all three cases. The “roll-up” effect of N_2 , whereby the outlet composition of N_2 was higher than its inlet value, until CO_2 broke through is clearly

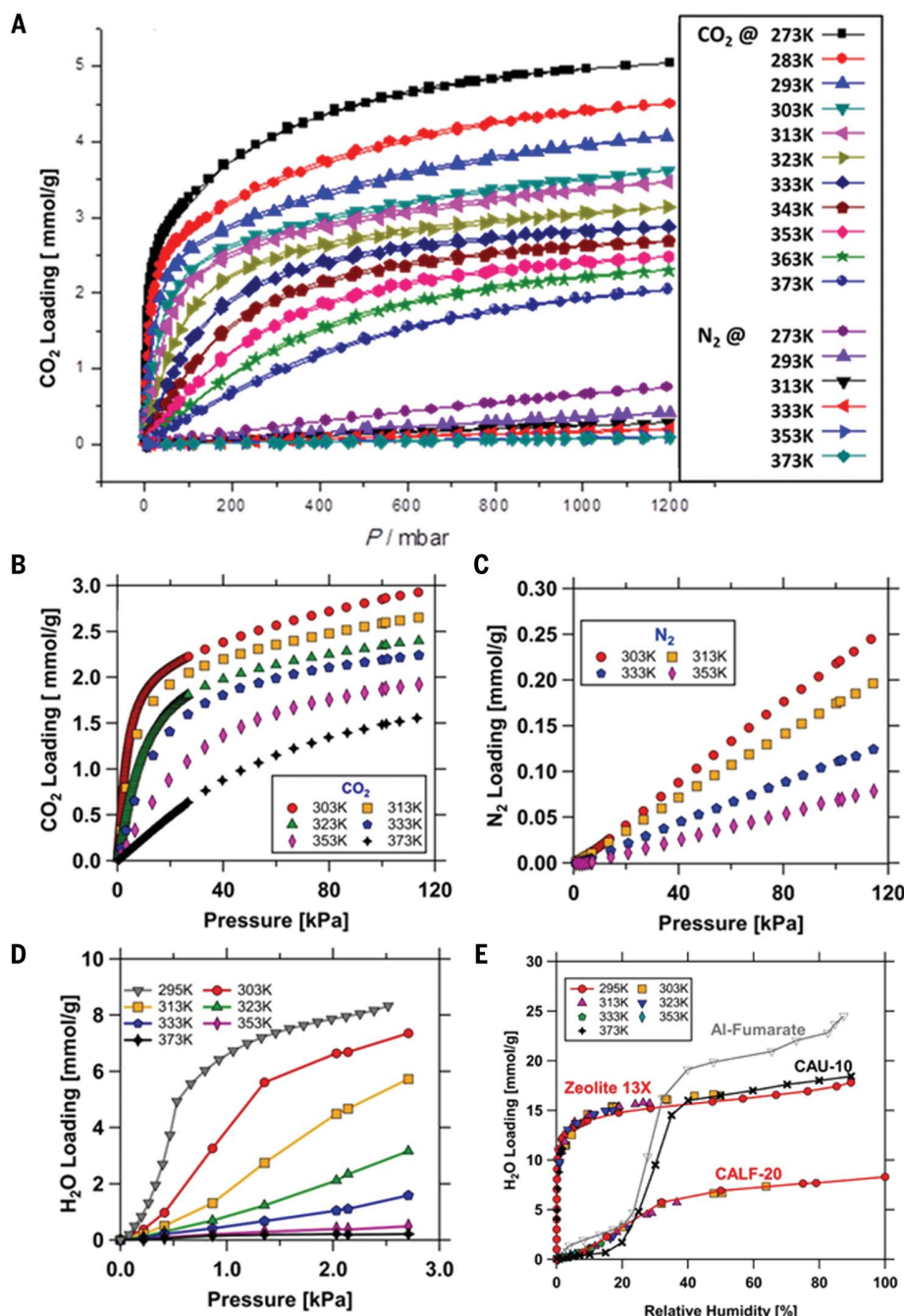


Fig. 2. Equilibrium gas uptake data on pure CALF-20. (A) CO₂ and N₂ isotherms from 273 to 373 K on pure CALF-20. (B to D) Structured CALF-20 (80% MOF:20% polysulfone). (B) CO₂ isotherms from 303 to 373 K. (C) N₂ isotherms from 303 to 353 K. (D) H₂O isotherms from 295 K to 373 K. (E) A comparison of H₂O isotherm on zeolite 13X (37), CAU-10 (38), Al fumarate (39) and structured CALF-20 at 295 K. The isotherms of CO₂ and N₂ were measured by volumetry, and that of H₂O was measured by gravimetry.

visible. The CO₂ concentration profiles showed different breakthrough times for various CO₂/N₂ compositions (Fig. 4A). Higher CO₂ composition in the feed led to shorter breakthrough times

We measured the competitive adsorption of CO₂ and H₂O using a combination of gravimetry, a study that measured the loading of CO₂ + H₂O by subjecting the sample to a moist

stream of CO₂ whose RH was controlled, and a breakthrough experiment that provided the competitive loading of H₂O in the presence of CO₂ (Fig. 4, B and C). The difference between the total loading from the gravimetry and the H₂O loading from the breakthrough provided the competitive CO₂ loading. Up to a value of 30% RH, the CO₂ loading was nearly unaffected (Fig. 4F), which was unexpected for a physisorptive

material but corroborated by the atomistic simulations. The CO₂ loading gradually decreased until it became negligible at RH > 80%. Additionally, the distinct shift in the H₂O isotherm in the presence of CO₂, compared to its pure-component isotherm, also confirmed the suppression of water sorption by CO₂.

To further demonstrate the physisorption of CO₂ by CALF-20 in wet environments, we measured the water breakthrough curves in air or CO₂ at two different RHs (Fig. 4, D and E). With the air experiment as a background, the water breakthrough was actually accelerated in CO₂, providing definitive support for the physisorptive preference of CALF-20 for CO₂ over water below 40% RH. The difference in water loading, exemplified by the area behind the breakthrough curve, between the two curves was pronounced. A comparison of both CO₂ and H₂O loading in competitive experiments (Fig. 4F and figs. S15 and S16) corroborated not only the sustained CO₂ capacity in wet gas but also the ability to suppress water sorption.

The nature of the water and CO₂ binding from the single-component water simulations and dry CO₂/N₂ simulations presented in Fig. 3 was consistent with the preferential binding of CO₂ over water observed at low RHs. Namely, CO₂ has strong binding sites in the center of the CALF-20 pores that precluded the formation of a hydrogen-bonded network that was responsible for the large uptake of water at high RHs. To corroborate this model, we performed multi-component simulations of CO₂, N₂, and water at varying RH. Figure S10 shows the comparison of simulated water uptake at various RHs from a single-component water simulation to that of multi-component simulations with 0.20 bar of CO₂ and 0.80 bar of N₂. The results were in good agreement with the experimental competitive isotherms shown in Fig. 4F. The simulations showed that without CO₂, water uptake at 20% RH is 6 mmol/g, whereas in the presence of CO₂, it was negligible. Only at 40% RH did water uptake reach 6 mmol/g when CO₂ was present. Calculated binding energies of most probable CO₂ and H₂O binding sites taken from the multi-component CO₂/N₂/H₂O simulations give $-17.5 \text{ kJ mol}^{-1}$ for H₂O and $-33.5 \text{ kJ mol}^{-1}$ for CO₂ (table S6). Calculated heats of adsorption, at zero loading and high loading (table S7), suggest that partially water-loaded pores were more attractive for subsequent water sorption than empty pores, and CO₂ had a stronger zero-loading heat of adsorption than water. A binding site analysis of the mixed CO₂/N₂/H₂O simulations is presented in the supplementary materials.

The low water-affinity yet CO₂-philic behavior of CALF-20 was enabled by its pore structure. Although a pore that is ideal for CO₂ is, of course, targeted in carbon capture, it is much less a focus that a pore be nonideal for water. Notably, a key feature of CALF-20 was the absence of any

strongly interacting functionality with CO₂. Although this property would be expected to moderate the affinity of the MOF for CO₂, the less specific dispersion interactions cumulatively compensate. As previously mentioned, dispersion interactions account for >85% of the binding energy in the most favorable CO₂ binding site. The boiling point of H₂O is 157°C higher than that of CO₂, so it is not expected that CO₂ would preferentially physisorb, but we can connect the competitive sorption in Fig. 4F with modeling in fig. S10. Interactions between guest molecules (40, 41), or in this case, the lack thereof as CO₂ blocked cooperative H₂O binding, could tip subtle balances in binding enthalpies. The pore itself is the critical element in performing a sorptive function (42). Other MOFs with low water affinity such as CAU-10 (38) and Al fumarate (39) have been reported and studied for CO₂ capture from wet gas. These MOFs have good CO₂/N₂ selectivity and reasonably low water affinity, as indicated by stepped water isotherms. However, CAU-10 loses CO₂ capacity above a RH value of 20%, and aluminum fumarate loses 17% CO₂ capacity at 14% RH (fig. S16). However, CALF-20 has a higher CO₂ capacity and retains it up to and beyond 40% RH. Also, neither shows the suppression of water sorption by CO₂ that is observed with CALF-20.

Flue gas sorption and scaling

Industrially, materials must absorb CO₂ from postcombustion flue gases at 100°C containing water vapor and acid gases, and endure stresses during regeneration as the sorbent goes through a temperature swing, pressure swing, or vacuum swing process. CALF-20 has been run through stability assessments from multiple academic, government, and industry partners and shows robust performance, as confirmed by retention of structure and gas adsorption properties. The retention of CO₂ capacity after being repeatedly heated to dry air at 150°C in the thermal gravimetric analysis (Fig. 5A) showed excellent stability (6, 43). This feature is key to high sorbent lifetime, as there is residual O₂ in the flue gas and during conditioning of the bed where air can oxidize reactive groups.

Powder x-ray diffraction (Fig. 5B) and N₂ sorption isotherms (Fig. 5C) are shown after a week of exposure to 150°C steam. CALF-20 was also tested for retention of structure and porosity (figs. S12 and S13) after treatment with 20 parts per million (ppm) SO₂ and 100 ppm NO_x at 20°C in separate experiments. We subjected CALF-20 to a real flue gas stream (50°C, flow of 100 cm³ min⁻¹) from natural gas combustion containing 7.3% H₂O, 7.1% O₂, 147 ppm CO, 78 ppm NO, and 13 ppm NO₂ (see supplementary materials, fig. S3, and table S4). Under these flowing flue gas conditions, powdered CALF-20 lost only 1.3% of its capac-

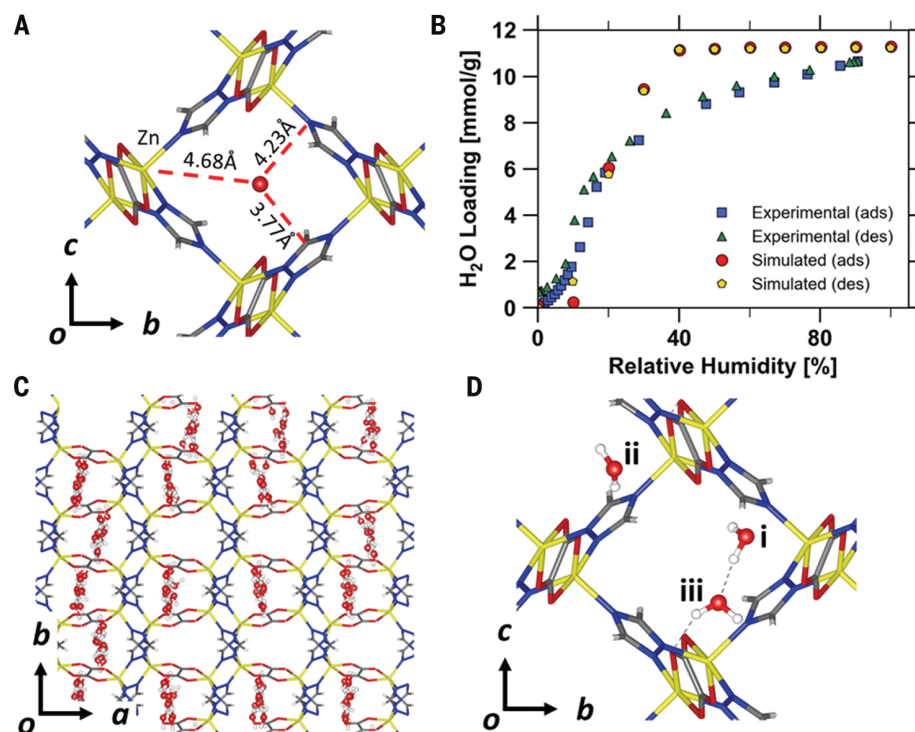


Fig. 3. Most probable CO₂ binding site determined from the single-component CO₂ GCMC simulation at 0.15 atm. (A) Select distances between heavy atoms of the CALF-20 framework and the CO₂ atoms are highlighted. These are the shortest distance between atoms of the framework and any atom of the CO₂ molecule. (B) Experimental and simulated single-component water isotherms at 293 K. Simulated adsorption results refer to the values obtained starting from empty pores, whereas the desorption results refer to the values obtained by starting the simulation with the pores saturated with water. (C) A snapshot from a 20% RH simulation of water in CALF-20. (D) The three most probable H₂O binding sites determined from the single-component water simulation at 20% RH. For (A), (C), and (D), ball-and-stick representations are used for the guest, whereas a tube representation is used for the framework. Atom colors are the same as shown in Fig. 1B.

ity after 6 days, as confirmed by gravimetric CO₂ uptake in a 15/85 mixture of CO₂/N₂. A process demonstration unit using the Svante VelloxTherm process was built on the basis of rotating beds and fast cycles (~1 min) at 0.1 tonne per day CO₂ capacity, and it was deployed to test the CALF-20 lifetime with simulated cement flue gas. This simulated flue gas was generated by enriching real flue gas from a natural gas boiler with pure CO₂ and air to bring CO₂, water, and O₂ concentrations to cement kiln flue gas composition (17% CO₂, 10% O₂, 5% H₂O, balance N₂, at 45°C). The gas analyzer recorded around 60 ppm NO and 12 ppm NO₂ in the generated flue gas that was fed to the CALF-20 beds. The process was continuously tested for over 2000 hours with expected key performance indicators and no appreciable performance loss, as can be seen in fig. S17 (44). Furthermore, the process was able to achieve US Department of Energy target CO₂ purity of 95%.

For large-scale applications, it is important that the scale-up be feasible from an economic and technical viewpoint (45). Analysis of the

cost driver for different MOF syntheses reveals that the costs of the raw materials, especially for the linker and less commonly for the metal, are often prohibitive. In addition, synthetic process conditions can have a substantial impact on the economics—for example, the necessity of high-pressure equipment is not only expensive but also results in costly safety precautions to protect employees and the environment. For CALF-20, none of these disadvantages apply (46). The raw materials are commercially available on a large scale from qualified vendors. Both linkers are low-cost bulk chemicals with large global production capacity (47): 200,000 metric tonnes per annum (MTPA) for oxalic acid, found mainly in pharmaceutical, textile and mining industries; 10,000 MTPA for triazoles, used mainly in the agricultural sector as a building block for azole-based fungicides. In addition, the reaction could be carried out in a water/methanol mixture, where the organic solvent represents <25 wt % with ongoing improvements. These conditions are particularly advantageous from a safety and environmental aspect. Further, in large-scale

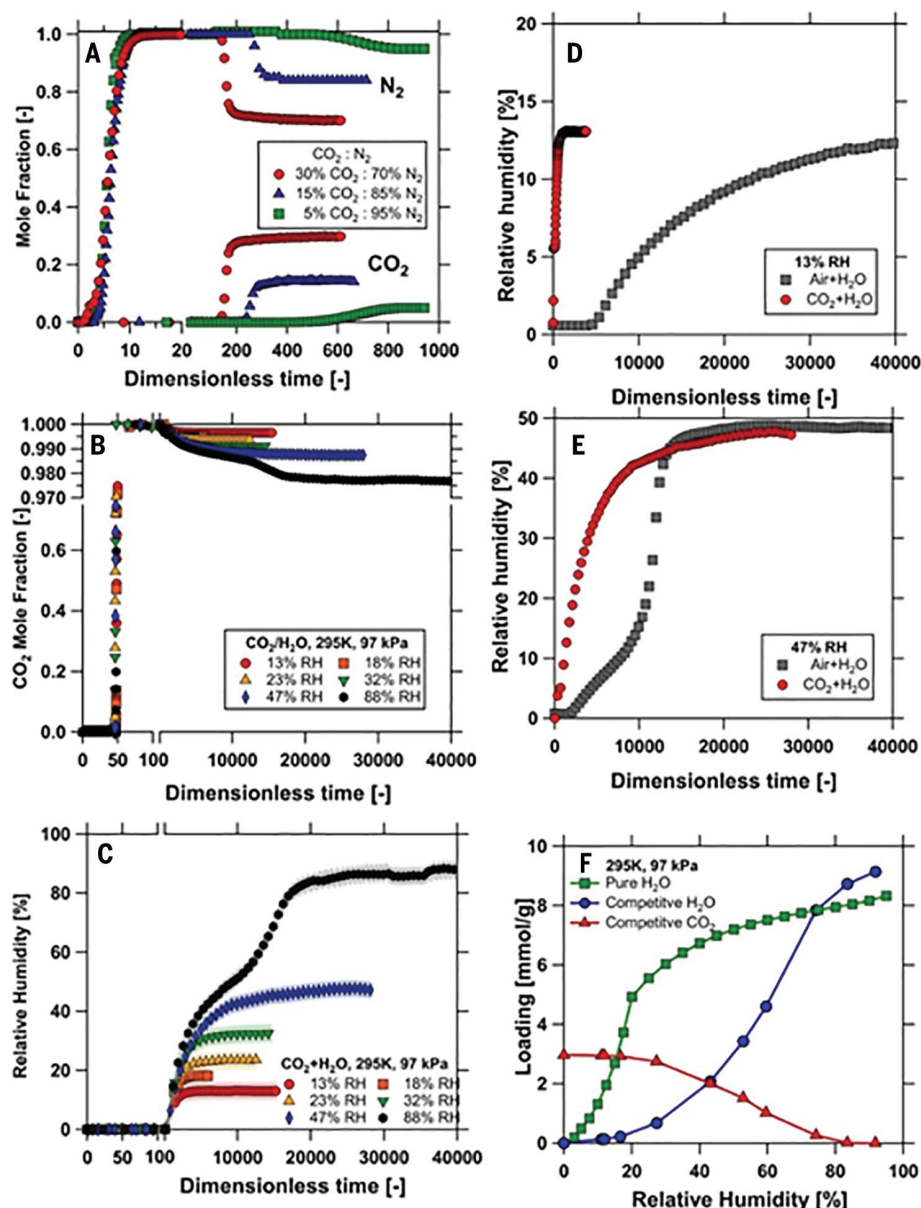


Fig. 4. Competitive dynamic column breakthrough (DCB) and equilibrium measurements on structured CALF-20 at 295 K and 97 kPa. (A) Competitive DCB of CO₂ and N₂ at different compositions. (B) Competitive CO₂ breakthrough curves measured at various RH values. (C) Competitive H₂O breakthrough curves at various RH values corresponding to the curves shown in (B). (D) A comparison of breakthrough curves obtained from experiments with Air + H₂O and that with CO₂ + H₂O at 13% RH. (E) A comparison of breakthrough curves obtained from experiments with Air + H₂O and that with CO₂ + H₂O at 47% RH. (F) Competitive CO₂ loadings (red triangle) and competitive H₂O loadings (blue circle) at various RH values. The loading of pure H₂O isotherm (green square) is shown as a reference. The breakthrough curves are plotted in dimensionless time, which is the ratio of the actual time to the average retention time taken of a nonadsorbed component. Also, there is a break in the abscissa of breakthrough curves.

batch synthesis, CALF-20 can obtain an unusually high solid content (total amount of dried MOF per total amount of solvents used) of >35%. The high yield of >90%, the reasonable reaction time, and the very high solid content result in an exceptional space-time yield (STY) for the precipitation step of

550 kg/m³ day. In comparison, the STYs for zeolites are in the range of 50 to 150 kg/m³ day (48). Critically, the CO₂ uptake of CALF-20 was retained through a wide range of scaling and structuring. Figure 5D shows a 3 million-fold difference in scale with matching CO₂ isotherms.

Outlook

An ideal adsorbent for the postcombustion CO₂ capture should exhibit several properties, including (i) high CO₂ adsorption capacity; (ii) fast adsorption/desorption kinetics; (iii) high CO₂ selectivity over N₂, O₂, and ability to function in wet gas; (iv) mild regeneration conditions; (v) the ability to be formed into structures, e.g., beads, laminates, or monoliths; (vi) chemical, mechanical, and thermal stability during adsorption-desorption cycling; and (vii) low cost and scalability of production. We have shown that CALF-20 can meet all of these criteria and help make industrial-scale CO₂ capture cost effective and reliable (44). Other MOFs have better reported properties in one or more of the aforementioned criteria, but not in all of them. For example, most reported MOFs cannot tolerate even ambient moisture or steam despite having very high CO₂ capacity or high CO₂/N₂ selectivity. The other important factor to consider is cost and scalability of synthesis. Most MOFs need aprotic solvents (such as dimethyl formamide or diethyl formamide) or contain expensive and noncommercial-grade organic linkers. With CALF-20, the components are commercially available at low cost and large volume, and water and methanol are the solvents used to synthesize this MOF.

In terms of gas separations, there is an increasing body of evidence showing that simple metrics such as selectivity and working capacity correlate poorly with ultimate process performance (49–53). A recent study that screened >5000 MOFs (54) showed that sorbent screening should include detailed process modeling and optimization. The Svante VeloxoTherm capture process used direct steam to rapidly desorb all the captured CO₂. In comparison to a traditional temperature swing process, the steam regeneration step of the VeloxoTherm process provided concentration swing in addition to heat, which allowed the extraction of the entire quantity of physisorbed CO₂, through its cyclic working capacity. Beyond steam stability, key aspects of the CALF-20 adsorbent synergizing with this process are its low water affinity and its ability to rapidly physisorb CO₂ in a wet gas, facilitating faster cycling, higher productivity, and ultimately resulting in a smaller plant footprint. In the Svante process with CALF-20, less energy is required to remove moisture in the drying cycle, and it also bears a higher moisture tolerance, which allows the capture cycle to recommence more rapidly.

Although materials can have one or more exceptional features, the key point is to merge those properties with process engineering conditions that best exploit them, such as capture conditions and available waste energy or heat for regeneration. The high uptakes at lower partial pressures of CO₂ make CALF-20

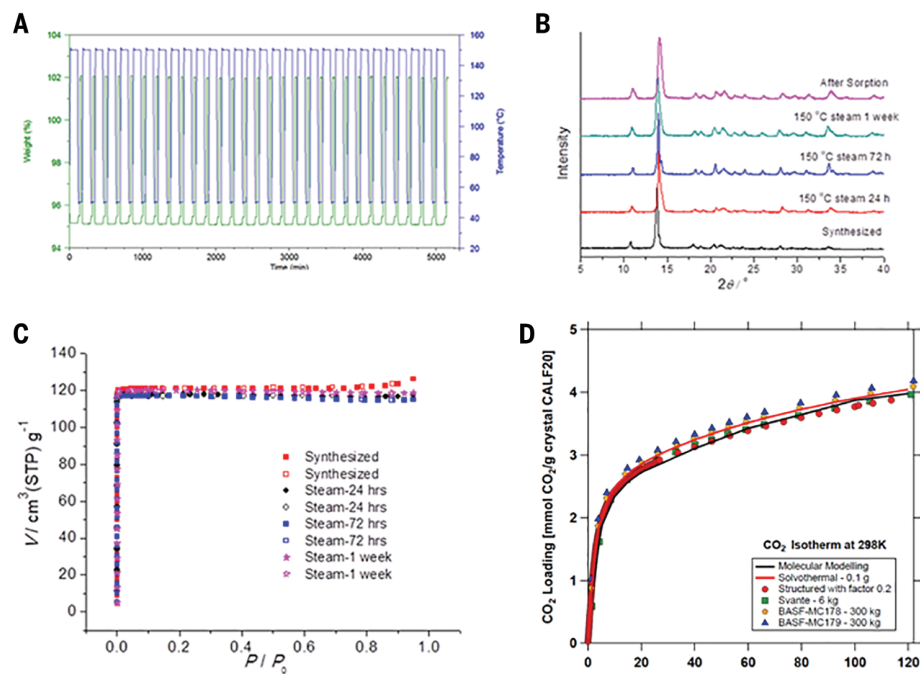


Fig. 5. CALF-20 scalability and stability. (A) Cycling of heating and introduction of CO₂ showing 30 cycles heated to 150°C. The left y axis is truncated to show the CO₂ mass gain on each cycle. CALF-20 survived more than 450,000 steam treatments in another test, but CO₂ uptake was only measured on the terminal sample. (B) Powder x-ray diffractograms and treatment with steam and running gas sorption shown in (C) N₂ isotherms at 77 K run on steam-treated samples and compared to pristine CALF-20. (D) CO₂ isotherms on 3 million-fold different scale batch preparations of CALF-20, showing retention of the CO₂ capacity. Comparisons with simulated uptake from the crystal structure and the structured CALF-20 scaled by a factor of 0.2 to account for 20% polysulfone are also shown.

a more suitable sorbent for a temperature or concentration swing process or potentially a pressure or vacuum swing at elevated temperatures. Independent of the regeneration process, the competitive nature of CO₂ and H₂O will enhance sorbent efficiency as coadsorption of water is reduced. Factoring its scalable preparation and durability, CALF-20 should derisk the use of MOFs for large-scale gas separation in industrial settings, and in particular, the challenge of postcombustion CO₂ capture (55, 56). In terms of carbon capture and climate change, efficient capture is only a step, albeit a very important one, in reducing greenhouse gases. With the integration of better materials into advanced processes, this derisking should lead to additional and larger demonstration projects for critical testing of MOFs in CO₂ capture and other strategic challenges.

REFERENCES AND NOTES

- "Accelerating Breakthrough Innovation in Carbon Capture, Utilization, and Storage" (U.S. Department of Energy, 2017).
- Z. Hu, Y. Wang, B. B. Shah, D. Zhao, *Adv. Sustainable Syst.* **3**, 1800080 (2018).
- K. Sumida et al., *Chem. Rev.* **112**, 724–781 (2012).
- B. Dutcher, M. Fan, A. G. Russell, *ACS Appl. Mater. Interfaces* **7**, 2137–2148 (2015).
- M. Wang, A. S. Joel, C. Ramshaw, D. Eimer, N. M. Musa, *Appl. Energy* **158**, 275–291 (2015).
- C. Gouedard, D. Picqa, F. Launay, P.-L. Carrette, *Int. J. Greenh. Gas Control* **10**, 244–270 (2012).
- M. Pardakhti et al., *ACS Appl. Mater. Interfaces* **11**, 34533–34559 (2019).
- L. A. Darunte, K. S. Walton, D. S. Sholl, C. W. Jones, *Curr. Opin. Chem. Eng.* **12**, 82–90 (2016).
- C. A. Trickett et al., *Nat. Rev. Mater.* **2**, 17045 (2017).
- A. E. Creamer, B. Gao, *Environ. Sci. Technol.* **50**, 7276–7289 (2016).
- J. C. Abanades et al., *Int. J. Greenh. Gas Control* **40**, 126–166 (2015).
- D. G. Madden et al., *Philos. Trans. A, Math. Phys. Eng. Sci.* **375**, 20160025 (2017).
- P. G. Boyd et al., *Nature* **576**, 253–256 (2019).
- E. González-Zamora, I. A. Ibarra, *Mater. Chem. Front.* **1**, 1471–1484 (2017).
- J. H. Cavka et al., *J. Am. Chem. Soc.* **130**, 13850–13851 (2008).
- A. J. Howarth et al., *Nat. Rev. Mater.* **1**, 15018 (2016).
- J. M. Kolle, M. Fayaz, A. Sayari, *Chem. Rev.* **121**, 7280–7345 (2021).
- S. Yuan et al., *Adv. Mater.* **30**, e1704303 (2018).
- J. Duan, W. Jin, S. Kitagawa, *Coord. Chem. Rev.* **332**, 48–74 (2017).
- E. J. Kim et al., *Science* **369**, 392–396 (2020).
- D. F. Sava Gallis, D. J. Vogel, G. A. Vincent, J. M. Rimsza, T. M. Nenoff, *ACS Appl. Mater. Interfaces* **11**, 43270–43277 (2019).
- S. Bhattacharyya et al., *Chem. Mater.* **30**, 4089–4101 (2018).
- G. W. Peterson, J. J. Mahle, J. B. DeCoste, W. O. Gordon, J. A. Rossin, *Angew. Chem. Int. Ed.* **55**, 6235–6238 (2016).
- P. A. Julien, C. Mottillo, T. Friscic, *Green Chem.* **19**, 2729–2747 (2017).
- S. Wang, C. Serre, *ACS Sustain. Chem. & Eng.* **7**, 11911–11927 (2019).
- M. Bui et al., *Energy Environ. Sci.* **11**, 1062–1176 (2018).
- R. B. Lin, D. Chen, Y. Y. Lin, J. P. Zhang, X. M. Chen, *Inorg. Chem.* **51**, 9950–9955 (2012).
- Y. Y. Lin, Y. B. Zhang, J. P. Zhang, X. M. Chen, *Cryst. Growth Des.* **8**, 3673–3679 (2008).
- X.-F. Wei, J. Miao, L.-L. Shi, *Synth. React. Inorg. Met.-Org. Nano-Met. Chem.* **46**, 365–369 (2016).
- S. R. Caskey, A. G. Wong-Foy, A. J. Matzger, *J. Am. Chem. Soc.* **130**, 10870–10871 (2008).
- J. An, S. J. Geib, N. L. Rosi, *J. Am. Chem. Soc.* **132**, 38–39 (2010).
- P. Nugent et al., *Nature* **495**, 80–84 (2013).
- T. M. McDonald et al., *Nature* **519**, 303–308 (2015).
- P. M. Bhatt et al., *J. Am. Chem. Soc.* **138**, 9301–9307 (2016).
- S. Nandi et al., *J. Am. Chem. Soc.* **139**, 1734–1737 (2017).
- S. Xiang et al., *Nat. Commun.* **3**, 954 (2012).
- N. S. Wilkins, J. A. Sawada, A. Rajendran, *Adsorption* **26**, 765–779 (2020).
- V. B. López-Cervantes et al., *Polyhedron* **155**, 163–169 (2018).
- J. A. Coelho et al., *Ind. Eng. Chem. Res.* **55**, 2134–2143 (2016).
- K. S. Walton et al., *J. Am. Chem. Soc.* **130**, 406–407 (2008).
- R. Vaidhyanathan et al., *Science* **330**, 650–653 (2010).
- S. Kitagawa, R. Matsuda, *Coord. Chem. Rev.* **251**, 2490–2509 (2007).
- M. Jahandar Lashaki, S. Khashiavi, A. Sayari, *Chem. Soc. Rev.* **48**, 3320–3405 (2019).
- P. Hovington, O. Ghaffari-Nik, L. Mariac, A. Liu, B. Henkel, S. Marx, Rapid Cycle Temperature Swing Adsorption Process Using Solid Structured Sorbent for CO₂ capture from Cement Flue Gas, Proceedings of the 15th Greenhouse Gas Control Technologies Conference, 15–18 March 2021.
- M. Rubio-Martinez et al., *Chem. Soc. Rev.* **46**, 3453–3480 (2017).
- J. M. Taylor, R. K. Mah, G. K. H. Shimizu, Synthesis of Zinc MOF Materials, PCT/CA2019/050530, filed 24 April 2019.
- S. N. Bizzari, M. Blagoev, CEH Marketing Research Report, *Chemical Economics Handbook*, SRI Consulting, April 2010.
- A. U. Czaja, N. Trukhan, U. Müller, *Chem. Soc. Rev.* **38**, 1284–1293 (2009).
- A. K. Rajagopalan, A. M. Avila, A. Rajendran, *Int. J. Greenh. Gas Control* **46**, 76–85 (2016).
- J. Park et al., *Ind. Eng. Chem. Res.* **59**, 7097–7108 (2020).
- K. T. Leperi, Y. G. Chung, F. You, R. Q. Snurr, *ACS Sustain. Chem. & Eng.* **7**, 11529–11539 (2019).
- M. Khurana, S. Farooq, *Ind. Eng. Chem. Res.* **55**, 2447–2460 (2016).
- A. H. Farmahini, S. Krishnamurthy, D. Friedrich, S. Brandani, L. Sarkisov, *Chem. Rev.* **121**, 10666–10741 (2021).
- T. D. Burns et al., *Environ. Sci. Technol.* **54**, 4536–4544 (2020).
- A. Samanta, A. Zhao, G. K. H. Shimizu, P. Sarkar, R. Gupta, *Ind. Eng. Chem. Res.* **51**, 1438–1463 (2012).
- R. L. Siegelman, E. J. Kim, J. R. Long, *Nat. Mater.* **20**, 1060–1072 (2021).

ACKNOWLEDGMENTS

Funding: This research was undertaken thanks in part to funding from Alberta Innovates Technology Futures (Strategic Research Grant), the Natural Sciences and Engineering Research Council (NSERC) of Canada (CREATE Grant), the US Department of Energy's (DOE) office of Fossil Energy (FE) DE-FOA-0001792, GreenSTEM from Alberta Jobs, Economy, and Innovation, Carbon Management Canada's Carbon Capture and Conversion Institute, MITACS, Innovate Calgary, the Canada First Research Excellence Fund (Global Research Initiative in Sustainable Low Carbon Unconventional Resources), and a Parex Innovation Fellowship to GKHS. We also thank Compute Canada for computing resources.

Author contributions: Methodology and Investigation: J.-B.L., T.T.T.N., R.V., J.M.T., N.J.F., R.K.M., O.G.-N., S.S.I., K.W.D., P.S., S.M.; Formal Analysis: J.-B.L., T.T.T.N., J.B., H.D., O.G.-N., A.R., T.K.W., G.K.H.S.; Funding acquisition/Supervision/Project administration: A.R., T.K.W., P.H., G.K.H.S.; Writing: J.-B.L., T.T.T.N., A.R., T.K.W., and G.K.H.S. wrote the first draft. All authors contributed to the final draft. **Competing interests:** Two patents (CA2904546A1 and EP3784824A1) related to CALF-20 are licensed to Svante Inc. and ZoraMat Solutions Inc. for different fields of use. J.-B.L., R.V., R.K.M., J.M.T., S.S.I., K.W.D., and G.K.H.S. receive royalties from the license. T.T.T.N., H.D., J.B., F.A., S.M., N.J.F., P.S., A.R., T.K.W. have no competing interests. **Data and materials availability:** The CIF file for CALF-20 is available at the Cambridge Crystallographic Data Centre with deposition number CCDC 2084733. All other data, excepting the large-scale synthesis of CALF-20, which is patent-pending, are available in the manuscript or the supplementary materials. Samples of CALF-20 are available for data reproduction purposes from BASF/Svante under a material transfer agreement via P.H. (phovington@svanteinc.com).

SUPPLEMENTARY MATERIALS

science.org/doi/10.1126/science.abi7281
Materials and Methods
Figs. S1 to S17
Tables S1 to S7
References (57–74)
26 March 2021; accepted 19 October 2021
10.1126/science.abi7281